Supporting Information for

Curvature-Selective Nanocrystal Surface Ligation Using Sterically-Encumbered Metal-Coordinating Ligands

Authors:

Yufei Wang[1,2]†, Amanda A. Chen[1]†, Krista P. Balto[3]†, Yu Xie[1], Joshua S. Figueroa[2,3*], Tod A. Pascal[1,2*], and Andrea R. Tao[1,2,3*]

Affiliations:

[1]Department of Nanoengineering and Chemical Engineering, 9500 Gilman Dr., University of California San Diego, La Jolla, CA 92023-0448

[2]Materials Science and Engineering Program, 9500 Gilman Dr., University of California San Diego, La Jolla, CA 92023

[3]Department of Chemistry and Biochemistry, 9500 Gilman Dr., University of California San Diego, La Jolla, CA 92023

[*] Email: jsfig@ucsd.edu, tpascal@ucsd.edu, atao@eng.ucsd.edu

† These authors contributed equally to this work.

S1. Materials and Methods.

S1.1. Chemicals and Materials

Sodium citrate (≥99%), sodium borohydride ($NaBH_4$, ≥98.0%), gold(III) chloride trihydrate ($HAuCl_4 \cdot 3H_2O$, ≥99.9%), hydroxylamine hydrochloride ($NH_2OH \cdot HCl$, 98%) and Xylyl isocyanide (CNXyl; Xyl = 2,6-$Me_2C_6H_3$; 98%) were purchased from Sigma-Aldrich and used as received. Water used in experiments was obtained from a Millipore water purification system with a resistivity of 18.2 MΩ cm. The *m*-terphenyl isocyanide ligands $CNAr^{Mes2}$ (Ar^{Mes2} = 2,6-(2,4,6-$Me_3C_6H_2)_2C_6H_3$) [1], $CNAr^{Dipp2}$ (Ar^{Dipp2}= 2,6-(2,6-(*i*-Pr)$_2C_6H_3)_2C_6H_3$); *i*-Pr = *iso*-propyl) [2], and $CNAr^{Tripp2}$ (Ar^{Tripp2}= 2,6-(2,4,6-(*i*-Pr)$_3C_6H_2)_2C_6H_3$) [3], were prepared as previously described.

S1.2. Synthesis of Citrate-Capped Gold Nanospheres (AuNSs)

Citrate-AuNSs with a diameter of 5 ± 0.7 nm were purchased from *nanoComposix Inc.* of San Diego, California.

Citrate-AuNSs 10 nm in diameter were synthesized according to the method of Bastús *et al*.[4] An aqueous solution of sodium citrate (150 mL, 2.2 mM) was refluxed under vigorous stirring in a 250 mL three-necked round-bottomed flask. The flask was equipped with a condenser to prevent solvent evaporation. An aqueous solution containing $HAuCl_4 \cdot 3H_2O$ (1 mL, 25 mM) was injected into the sodium citrate solution and heating was continued for an additional 20 min. The resulting colloidal solution of AuNSs were used directly for further experiments and TEM imaging. The synthesized 10 nm citrate-AuNSs had a measured diameter of 11.5 ± 1 nm based on TEM images (**Fig. S1**).

Citrate-AuNSs of 20 nm in diameter were synthesized in a modified Turkevich method.[5] An aqueous solution containing $HAuCl_4 \cdot 3H_2O$ (5 mg, 0.015 mmol, 0.3 mM) was refluxed under vigorous stirring. A aqueous solution containing sodium citrate (5 mL, 0.23 mmol, 46.5 mM) was injected into the boiling solution. The solution was heated for an additional 30 min and cooled to room temperature before further use. The resulting colloidal solution of AuNSs were used directly for further experiments and TEM imaging. The synthesized 20 nm citrate-AuNSs had a measured diameter of 22 ± 2 nm based on TEM images (**Fig S1**).

The 20 nm AuNSs were used as-synthesized as seed particles to synthesize AuNSs of 50 nm in diameter. An aqueous solution of the seed particles (20 nm AuNPs, 3.0 mL) and $NH_2OH \cdot HCl$ (200 µL, 0.2 M) were added to 50 mL water in a 100 mL round-bottom flask. $HAuCl_4 \cdot 3H_2O$ (3.0 mL of 0.1 wt% solution in H_2O) was added dropwise to the solution under vigorous stirring and allowed to react for 30 min at room temperature. A gradual color change from light to dark red was observed. The 50 nm citrate-AuNS had a measured diameter of 56 ± 6 nm measured based on TEM images (**Fig. S1**). The AuNSs of 80 nm and 100 nm diameter were synthesized by the same seeded-growth method as the 50 nm particles. For AuNSs of 80 nm diameter, 2.0 mL seed solution was used, whereas 1.0 mL of seed solution was used to prepare AuNSs of 100 nm diameter. The resulting colloidal solution of AuNSs were used directly for further experiments and TEM imaging. The 80 nm citrate-AuNS had diameter of 80 ± 7 nm and 100 nm nanospheres had diameter of 105 ± 10 nm as measured from TEM images (**Fig. S1**).

All gold dispersion concentrations were adjusted to maintain the same overall molar concentration of surface atoms, which is estimated to be approximately 10^{16} atoms/mL. Using UV-Vis spectroscopy, optical density measurements were performed to calculate the amount of surface gold atoms per mL (**Fig. S3, Fig. S11**). Assuming a AuNS has perfect spherical shape in the fcc habit, the surface atom number per AuNS (*N*) was calculated by:

$$N = \frac{\frac{4}{3}\pi[(\frac{D}{2})^3 - (\frac{D}{2} - D_{Au})^3]}{V_{Au}} \cdot n_{fcc} \ , \quad \text{Eq. (1)}$$

where D is the average diameter of the AuNSs, D_{Au} is the average diameter of gold atom, V_{Au} is the volume of one Au unit cell and n_{fcc} is the number of Au atoms per one unit cell. The concentration of the AuNSs in water (c) was calculated by:

$$c = \frac{OD}{\varepsilon} \ , \quad \text{Eq. (2)}$$

$$\varepsilon = \frac{N_A}{\ln(10)} \cdot C_{ext} \ , \quad \text{Eq. (3)}$$

$$C_{ext} = C_{ext} \cdot \pi r^2 \ , \quad \text{Eq. (4)}$$

where OD is the optical density measured by UV-Vis spectroscopy, ε is the molar extinction coefficient, N_A is Avogadro's constant, C_{ext} is the extinction cross-section, πr^2 is the cross-sectional area of the NP, Q_{ext} is the extinction efficiency obtained from the reference Liu *et al.*[6]

S1.3. Liquid-Liquid Extraction (LLE) of AuNS with Isocyanide Ligands

An aqueous dispersion of AuNSs (3.0 mL, 10^{16} atoms/mL) was layered onto a chloroform solution containing isocyanide (1.0 mL, 15 mM) in a glass vial. After layering the aqueous AuNSs dispersion onto the organic solution, the two-phase system was mixed vigorously by hand for 30 min. The aqueous layer was decanted, and the red-colored organic phase was washed with chloroform to remove excess free ligand in solution via centrifugation. The concentration of isocyanide was optimized by evaluating the extraction efficiency (**S1.2.**) of 20 nm AuNSs functionalized with $CNAr^{Mes2}$ and found to be 10 mM (**Fig. S11**). To guarantee successful ligand exchange, the concentration of isocyanide used in the LLE process was increased to 15 mM.

S1.4. Nanocrystal Characterization

Transmission electron microscopy (TEM) images were collected using a ThermoFisher Talos 200X TEM with an operation voltage of 200 kV. Samples were prepared by drop-casting AuNP solutions on copper grids and allowed to settle overnight in closed vials (Fig. S2). UV–visible absorption measurements were performed on Cary 50/60 UV-Vis spectrophotometer. Raman measurements were performed on Renishaw micro-Raman spectrometer (Renishaw Invia) coupled with a Leica microscope with 50× objective (Leica N-plan) in the range of 800−2400 cm^{-1}. A wavelength of 532 nm was used as an excitation source generated by 50 mW Ar-Ion LASER. Zeta potential values were measured using a Malvern NANO-ZS90 Zetasizer.

S1.5. Calculating the Change of Citrate-AuNSs Optical Density

The extraction efficiency for AuNSs with the isocyanide ligands is calculated based on the following equation:

$$Extraction\ efficiency = (1 - \frac{OD_{Raffinate}}{OD_{feedstock}}) \cdot 100\%, \quad \text{Eq. (5)}$$

where $OD_{raffinate}$ *and* $OD_{feedstock}$ are the optical density of citrate-AuNSs in water before and after the LLE measured by UV-Vis spectroscopy.

S1.6. Calculation of the equilibrium distribution coefficient (*D*)

The equilibrium distribution coefficient for extraction of the AuNSs into chloroform by $CNAr^{Mes2}$ binding is calculated using the following equation:

$$Equilibrium\ distribution\ coefficient\ = \frac{OD_{CHCl3}}{OD_{feedstock}} \cdot 100\%, \quad \text{Eq. (6)}$$

where $OD_{feedstock}$ is the optical density of citrate-AuNSs in water after the LLE measured by UV-Vis spectroscopy and OD_{CHCl3} is the optical density of citrate-AuNS in chloroform after the LLE calculated by subtracting $OD_{feedstock}$ from $OD_{raffinate}$.

S1.7. Calculation of Size Separation Efficiency of $CNAr^{Mes2}$

The separation efficiency for a mixture of two different sized AuNSs is calculated based on the number of larger sized AuNSs in water before and after LLE using the following equation:

$$Separation\ power = (1 - \frac{C_{Raffinate}}{C_{feedstock}}) \cdot 100\%\ , \quad \text{Eq. (7)}$$

where $C_{feedstock}$ is the concentration of the larger sized AuNS in the mixture before LLE and $C_{raffinate}$ is the concentration of larger sized AuNSs remaining in the aqueous phase after LLE. These concentrations are calculated from the optical density measured by UV-Vis spectroscopy (**Fig. S7**). Separation resolution was determined by taking the minimum size difference between the AuNSs being separated (e.g. extraction of 10 nm AuNSs from the 10/50 nm mixture) for separation efficiencies of >50% using our LLE method, as depicted in **Fig. 3D**.

S2. Computational Details.

Both Quantum Mechanics (QM) calculations and Molecular Dynamics (MD) simulations were used to study the binding thermodynamics and kinetics of the various ligands to the Au nanosphere surfaces. QM calculations were performed using the Q-Chem 5.2,[7] and Quantum Espresso (QE) [8-9] electronic structure packages to determine the optimized ligand structure and the ligand-gold interaction energies, respectively. The MD simulations were performed with LAMMPS [10] simulation engine. In MD, the Au nanoparticles were described using EAM/Fs potential of Ackland et. al. [11]. Ligands were described using either the GAFF [12] or OPLS/AA [13] forcefields, except for the critical C≡N bond stretching and the aromatic rings torsions, which were determined from QM to reproduce the CNXyl and $CNAr^{Mes2}$ intra-molecular motion. The $CHCl_3$ solvent was modelled using the Kamath et al. forcefield [14], while the SPC/E potential was used for water [15].

S2.1. Parameterization of the ligand C≡N/AuNS Interactions

Au-ligand(s) interaction was optimized by developing a forcefield based on fitting the binding energy curves obtained from QM calculations. The ligand(s) structure was first at the 6-31G/MP2 level using DFT using Q-Chem. Various Au slabs were constructed from the fcc crystal structures and the binding energy of the rigid ligand in QE was calculated with ultrasoft pseudopotentials [16], a kinetic energy cutoff of 30 Ry, and a (5,5,1) K-point grid. In each case, a ligand was initially placed far from the Au slab and gradually moved onto the Au slab. The energy vs distance curve for the various ligand(s)|Au configurations were obtained. The associated binding energy curve was further fitted to Lennard-Jones 12-6 / Morse potentials in determining the ligand(s) atoms | Au atoms interaction parameters, using a nonlinear regression approach.

S2.2. Description of System used in MD Simulations

A Chamfered cube AuNS with 4033 atoms was constructed containing equal edge lengths of 12 hexagons and 6 squares faces. (**Fig. S12**) The system was solvated by inserting the AuNS into a 100 x100 x 100 $Å^3$ box of $CHCl_3$ molecules and removing the solvent molecules within 2 Å of the AuNS. Afterwards, ligands were then distributed randomly in the simulation box and overlapping solvent molecules were removed as necessary. The vacuum systems (**Fig. 1B** and **Fig. S15**), did not contain $CHCl_3$ solvent and the simulation box was set as 100x100x100 $Å^3$. The composition of the various systems is detailed in **Table S4**.

S2.3. Equilibrium MD Simulations and Vibrational Spectral Analysis

The van der Waals and real space coulomb cutoffs in the MD simulations were 10Å. A cubic spline was applied to the van der Waals to ensure smooth convergence and vanishing energies and forces at the cutoff (inner cutoff distance of 9Å). The reciprocal space coulomb interactions were computed with a particle-particle-particle-mesh solver, with an error tolerance of 10^{-6} [17]. Each MD simulation was initiated with 500 conjugated gradient steps, followed by gradual heating to 298K using 0.5 ns (500,000 steps with an integration timestep of 1 fs) dynamics in the canonical ensemble (NVT – constant number of particles N, volume V and temperature T) at 298K. A Nose-Hoover thermostat was used with a temperature relaxation window of 100 fs. Afterwards, the system was equilibrated at the correct density by performing dynamics in the iso-baric isothermal (NPT: constant N, pressure P and temperature T) ensemble. The Shinoda et al. [18] equations of motion, which incorporates the Martyna et al[19] hydrostatic equations and the strain energy formulism of Parrinello and Rahman [20] were adopted. The time-reversible measure-preserving Verlet integrators derived by Tuckerman et al. [21] was applied for the time integration. After density equilibration, the system was simulated in the NVT ensemble for at least 5ns of NVT dynamics. Starting with snapshots of each system every 1 ns, additional 40 ps NVT simulation were run, and the velocities and coordinates were saved every 4 fs (10,000 frames in the corresponding trajectory). The vibrational density of states function was calculated, based on Fourier transform of the velocity autocorrelation functions, to analyze the ligand C≡N spectra (**Fig. S13)** [22-23].

S2.4. Radial Distribution Function Analysis

The radial distribution function, g(r), was used to calculate the ligand densities at various distance from the AuNS center of mass. The g(r) can be expressed as:

$$g(r) = \frac{d\left\langle N_{ij}(r)\right\rangle}{\rho_{ij} dV(r)} \qquad \text{Eq. (8)}$$

where $dV(r)$ is the volume of the shell being considered $d\langle N_{ij}(r)\rangle$ is the average number of either atom in $dV(r)$ within a distance dr of the other atom and r_{ij} is the atomic bulk density factor. In this analysis, the AuNS and each ligand molecule were taken as individual super atoms defined by the respective centers of mass and the closest contact point for each ligand is defined by the radius of the AuNS, ~ 25 Å.

S2.5. Ligand Solvation Free Energy Calculations

Free Energy Perturbation (FEP), based on the advancements of Zwanzig [24], is a statistical approach to compute the free energy difference between two states:

$$\Delta A \text{ (from state1 to state2)} = A \text{ (state2)} - A \text{ (state1)} = -k_B T \ln\left\langle \exp\left(-\frac{U(state2) - U(state1)}{k_B T} \right) \right\rangle \qquad \text{Eq. (9)}$$

where A denotes free energy, k_B is the Boltzmann constant, and U is energy.

The solvation energies of the various isocyanide ligands were calculated as the sum of multi-stages free energy changes. Here, a coupling parameter λ ($0 \leq \lambda \leq 1$) is introduced to gradually change the ligand – solvent interaction energy, such that the free energy [25] is obtained as:

$$\Delta_0^1 A = \sum_{i=0}^{n-1} \Delta_{\lambda_i}^{\lambda_{i+1}} A = -kT \sum_{i=0}^{n-1} \ln \left\langle \exp\left(-\frac{U(\lambda_{i+1}) - U(\lambda_i)}{kT} \right) \right\rangle_{\lambda_i} \qquad \text{Eq. (10)}$$

In this study, λ = 0.01 was used and the interaction energies were modified in 100 stages (windows) over 100 ps NPT per window. These results are presented in **Table S2**.

S2.6. Free Energy of Isocyanide Binding to Solvated AuNSs

Using accelerated MD simulations, the free energy kinetics of isocyanide ligand binding to AuNS was computed. Metadynamics [26] was employed to enhance the sampling and explore regions of the potential energy surfaces characterized by deep local minima. Two types of systems were considered: 1) a Au (100) slab, representative of the larger NPs with large radius of curvatures and 2) an edge site comprising a Au(110) motif on the Au (100) slab, representative of smaller NPs with small radius of curvatures (**Fig. S14**). Each system was first solvated and equilibrated according to the procedure above. Afterwards, Metadynamics simulations, where the carbon of the isocyanide group (C≡NR) to the Au surface was chosen as the collective variable (colvar), were performed. Each simulation was biased by depositing Gaussian functions every 0.2 ps with a height of 0.02 kcal/mol and a width of 1.25 Å. The system was evolved for a minimum of 200 ns. Convergence was checked by monitoring colvar distance until it showed ballistic behavior.

S2.7. Computation of Normalized Descriptors

To straightforwardly compare the binding and solvation energies, DFT interaction energies were corrected for zero-point energy (ZPE) and entropy of binding (TΔS) effects:

$$\Delta G_{DFT-bind} = \Delta E_{DFT-bind} + \Delta ZPE + T\Delta S \qquad \text{Eq. (11)}$$

where the ΔZPE is obtained from vibrational frequency calculations of the isolated and bound isocyanides, and TΔS is taken as difference between the free (ideal gas) and bound isocyanides. Generally, it was found that these corrections account for ~ +0.2 eV for the various structures.

For the various descriptors (X), relative energies (ΔY) were calculated and divided by the norm of the largest value if it exceeds 1:

$$X = \frac{\Delta Y}{\max|\Delta Y|} \qquad \text{Eq. (12)}$$

The various descriptors thus range from -1 (unfavorable) – +1 (favorable), with a favorable/unfavorable threshold taken as 0:

$$
\begin{aligned}
SBR &= \Delta G^{flat}_{DFT-bind} - \Delta G^{edge}_{DFT-bind} \\
EBF &= \Delta G^{edge}_{DFT-bind} - \Delta G^{CHCl3}_{solvation} \\
SF &= \Delta G_{cohesive} - \Delta G^{CHCl3}_{solvation} \\
SPF &= \Delta G^{H2O}_{solvation} - \Delta G^{CHCl3}_{solvation}
\end{aligned}
\qquad \text{Eq. (13)}
$$

where SBR is site binding ratio, EBF is edge-binding factor, SF is solubility factor and SPF is solvent partition factor.

S3. Supplementary Figures.

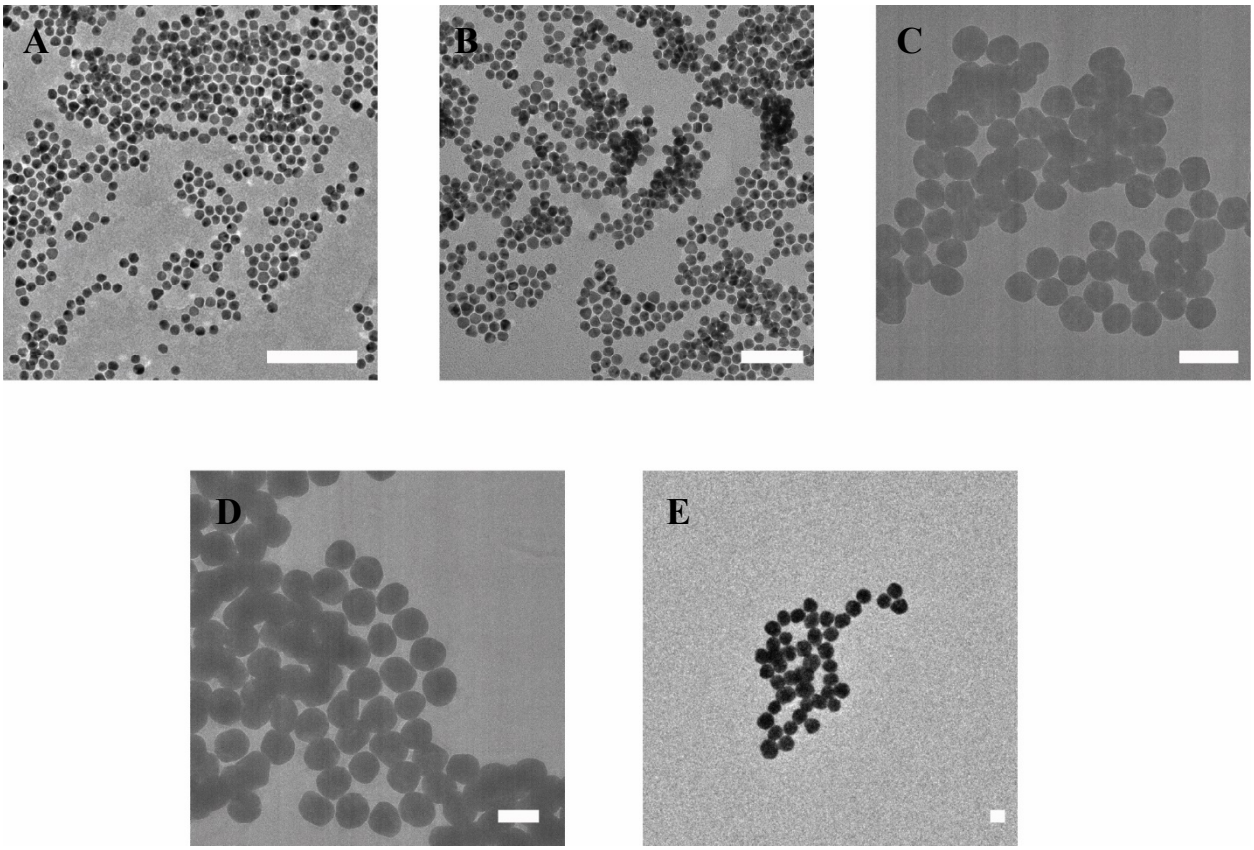

Fig. S1. TEM images of as synthesized (A) 10 nm, (B) 20 nm (C) 50 nm (D) 80 nm and (E) 100 nm diameter AuNSs before LLE (scale bar 100 nm).

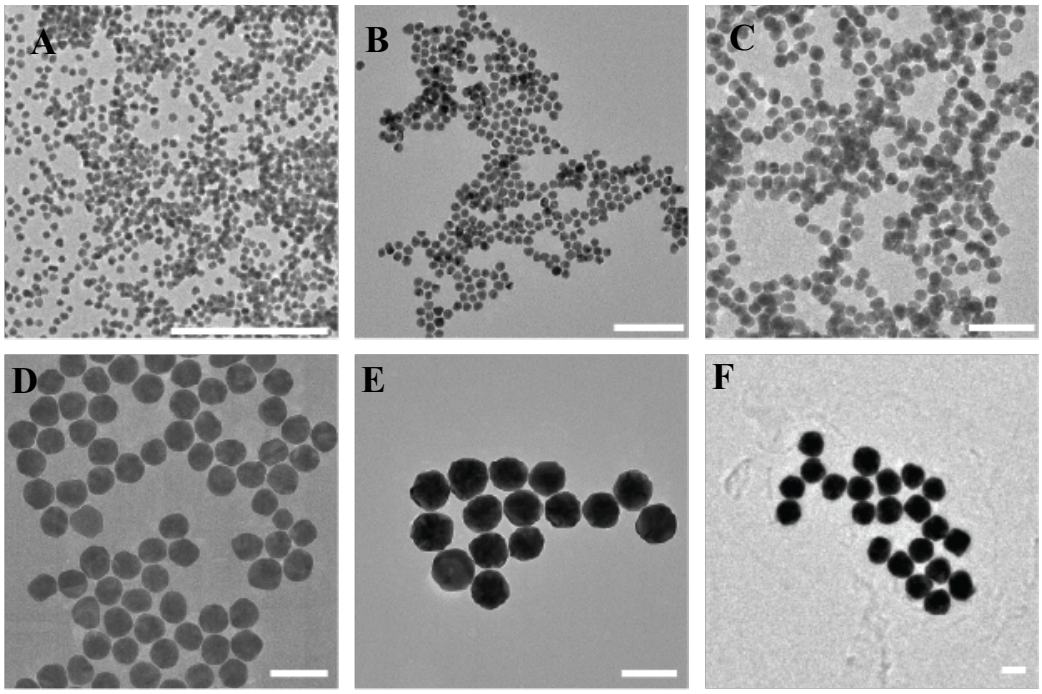

Fig. S2. TEM images of (A) 5 nm, (B) 10 nm, (C) 20 nm (D) 50 nm (E) 80 nm and (F) 100 nm diameter AuNSs transferred into $CHCl_3$ after LLE with $CNAr^{Mes2}$ (scale bar 100 nm).

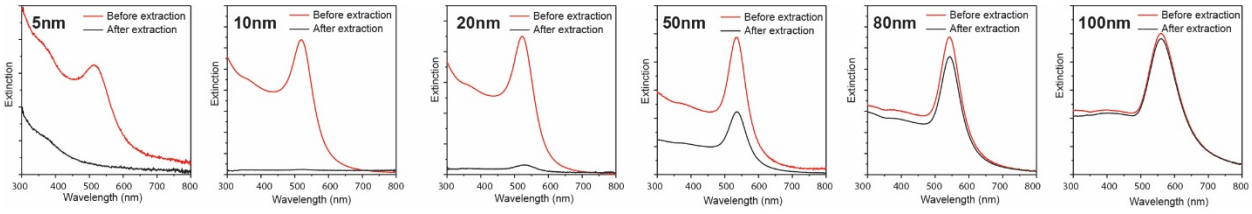

Fig. S3. UV-Vis spectra used to calculate $CNAr^{Mes2}$–LLE extraction efficiency of (left to right) 5 nm, 10 nm, 20 nm, 50 nm, 80 nm and 100 nm AuNSs. Red spectra represent the aqueous AuNS feedstock prior to introduction of $CNAr^{Mes2}$ in $CHCl_3$. Blue spectra represent the aqueous raffinate after introduction of $CNAr^{Mes2}$ in $CHCl_3$.

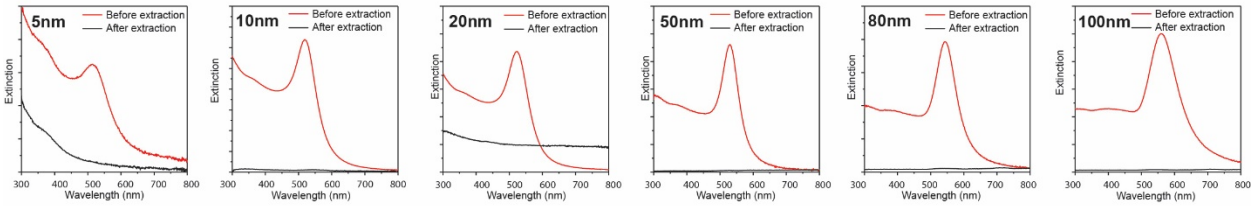

Fig. S4. UV-Vis spectra used to calculate CNXyl–LLE extraction efficiency of (left to right) 5 nm, 10 nm, 20 nm, 50 nm, 80 nm and 100 nm AuNSs. Red spectra represent the aqueous AuNS feedstock prior to introduction of CNXyl in $CHCl_3$. Blue spectra represent the aqueous raffinate after introduction of CNXyl in $CHCl_3$.

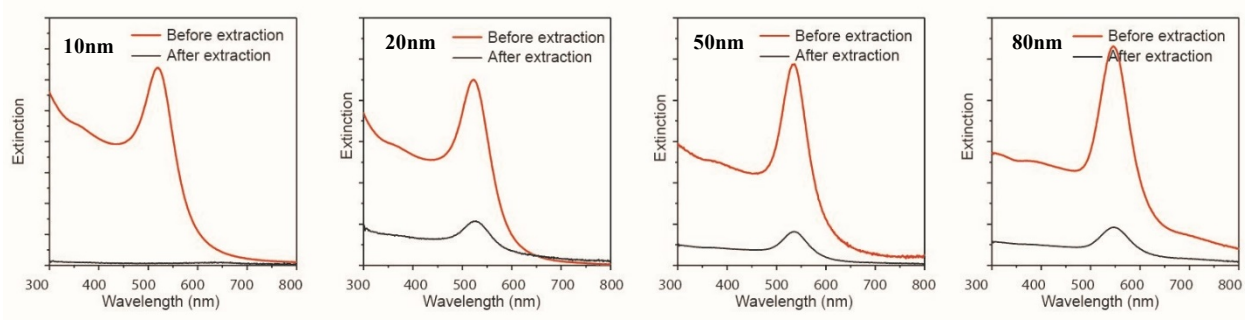

Fig. S5. UV-Vis spectra used to calculate $CNAr^{Dipp2}$–LLE extraction efficiency of (left to right) 10 nm, 20 nm, 50 nm and 80 nm AuNSs. Red spectra represent the aqueous AuNS feedstock prior to introduction of $CNAr^{Dipp2}$ in $CHCl_3$. Blue spectra represent the aqueous raffinate after introduction of $CNAr^{Dipp2}$ in $CHCl_3$.

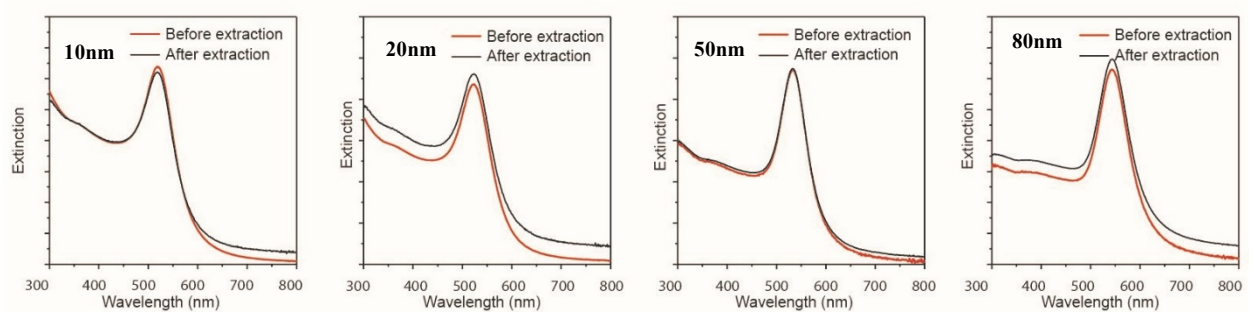

Fig. S6. UV-Vis spectra used to calculate $CNAr^{Tripp2}$–LLE extraction efficiency of (left to right) 10 nm, 20 nm, 50 nm and 80 nm AuNSs. Red spectra represent the aqueous AuNS feedstock prior to introduction of $CNAr^{Tripp2}$ in $CHCl_3$. Blue spectra represent the aqueous raffinate after introduction of $CNAr^{Tripp2}$ in $CHCl_3$.

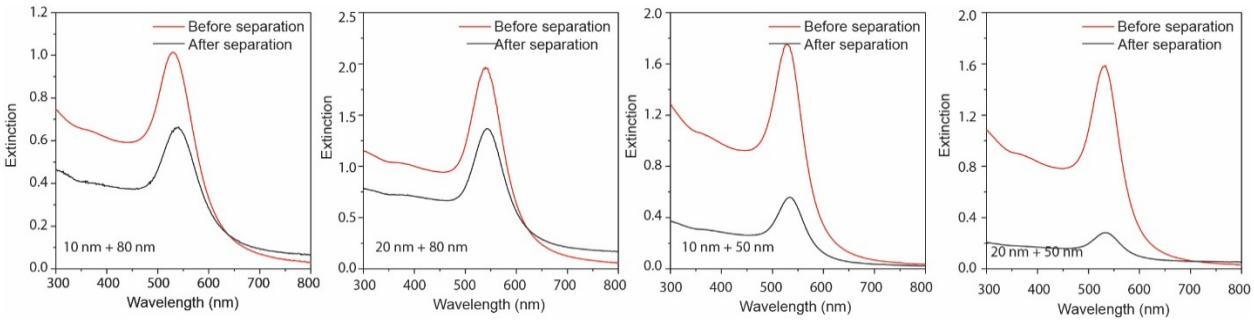

Fig. S7. UV-Vis spectra of AuNS mixtures prior to (red) and after (blue) introduction of $CNAr^{Mes2}$ in $CHCl_3$. (left to right): 10 nm and 80 nm AuNS mixture; 20 nm and 80 nm AuNS mixture; 10 nm and 50 nm AuNS mixture; 20 nm and 50 nm AuNS mixture.

5

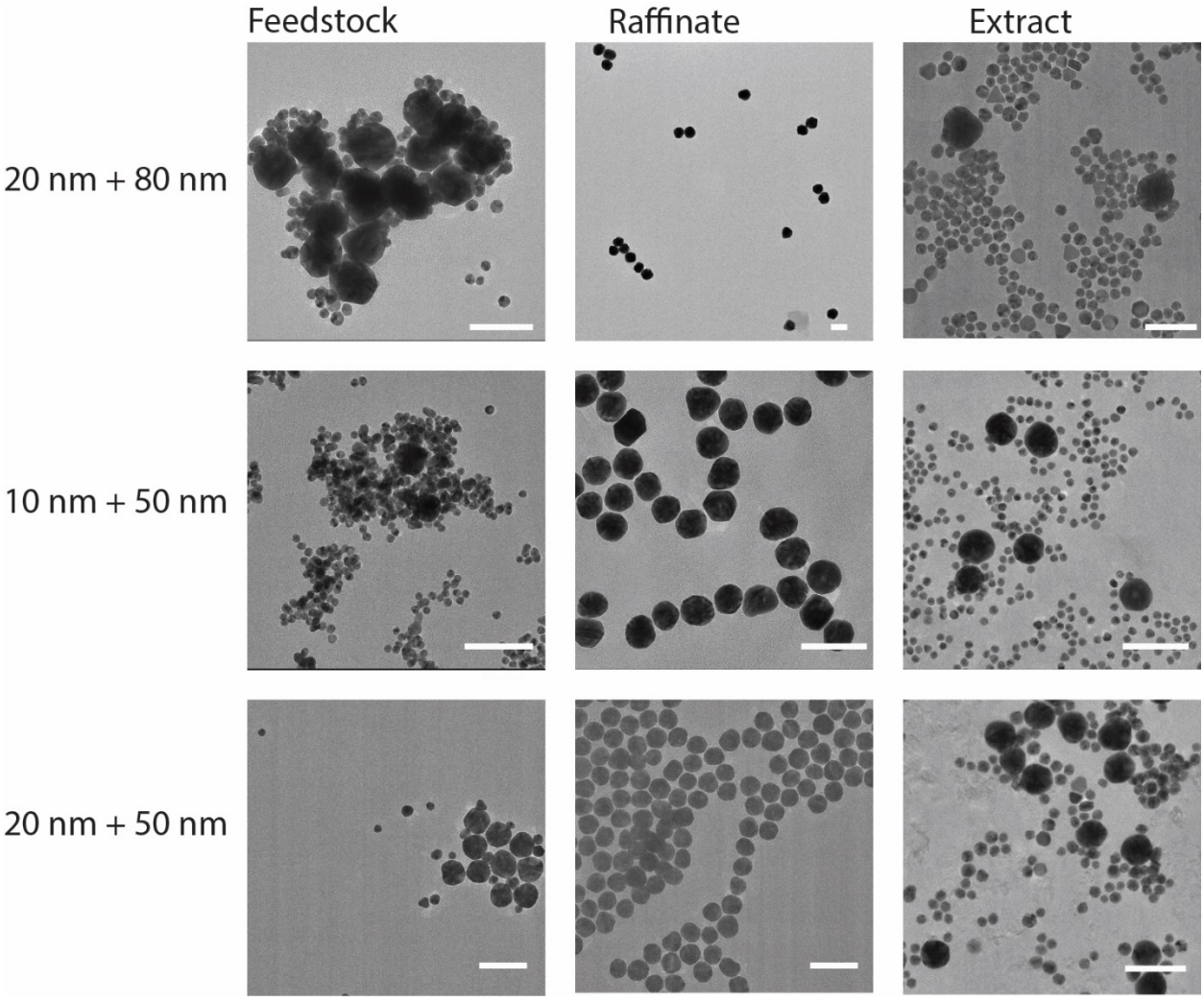

Fig S8. TEM images of AuNSs mixtures before (feedstock) and after (raffinate, extract) LLE with $CNAr^{Mes2}$ (scale bar 100 nm).

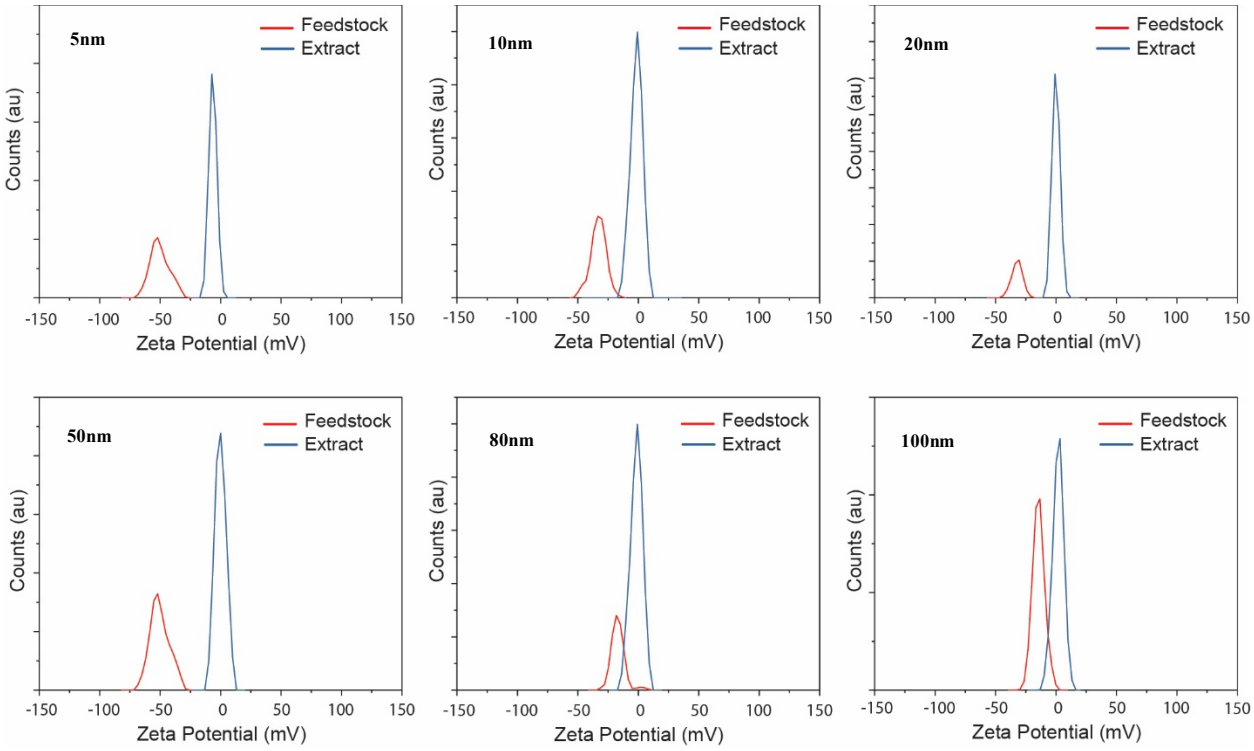

Fig. S9. Zeta potential plots of various sized AuNSs before (red) and after LLE (blue) with $CNAr^{Mes2}$.

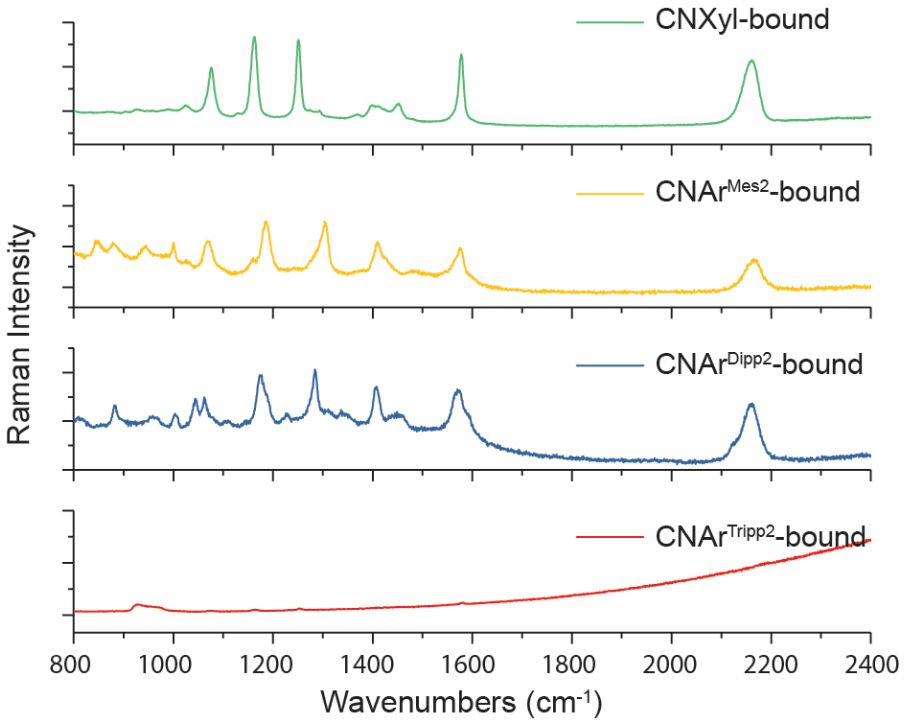

Fig. S10. SERS spectra of 10 nm AuNSs upon binding of isocyanide ligands. Binding of isocyanide ligands CNXyl, $CNAr^{Mes2}$, and $CNAr^{Dipp2}$ to AuNSs is indicated by the ν(CN) band at ~2165 cm^{-1}. A ν(CN) band is not observed for $CNAr^{Tripp2}$, thereby suggesting it does not readily bind to AuNSs, including ones with high curvature.

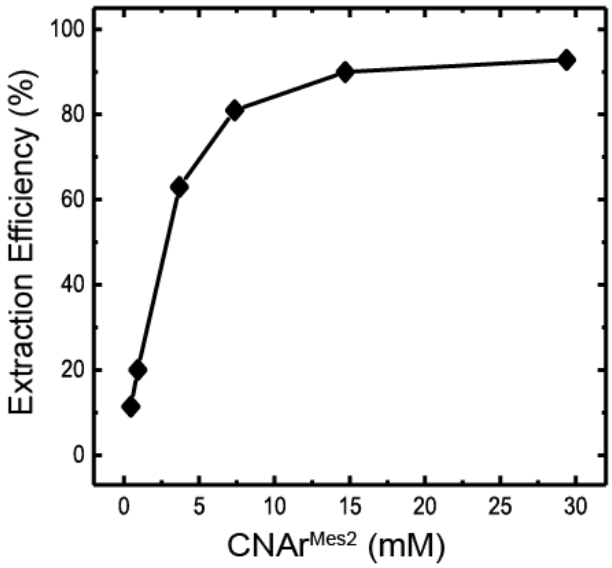

Fig. S11. Optimization of $CNAr^{Mes2}$ concentration used in LLE of 20 nm diameter AuNSs, where the x-axis is the concentration of $CNAr^{Mes2}$ in $CHCl_3$ and the y-axis is extraction efficiency calculated based on the change of optical density (**S1.5**). Optimal $CNAr^{Mes2}$ concentration was found to be 10 mM.

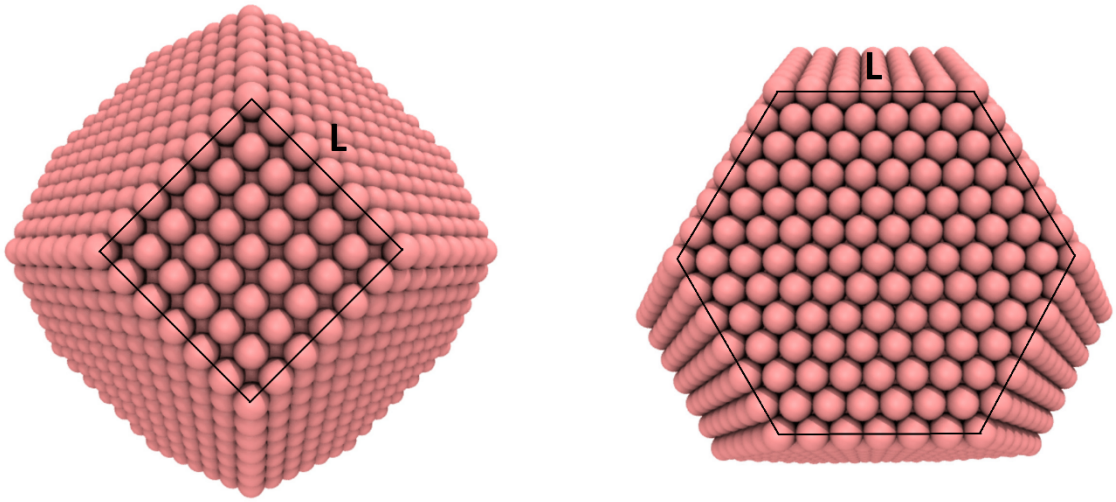

Fig. S12. Initial AuNS structure used in MD simulations. The diameter is ~5 nm and edge length, L, is ~1.7 nm. The distances from the AuNS center of mass to the Au(001) surfaces, the Au(111) surfaces, the Au(001/111) edges, the Au(111/111) edges, and the corners of Au(001/111/111) facets, are 24.5 Å, 21.5 Å, 26 Å, 26 Å, 27 Å, respectively.

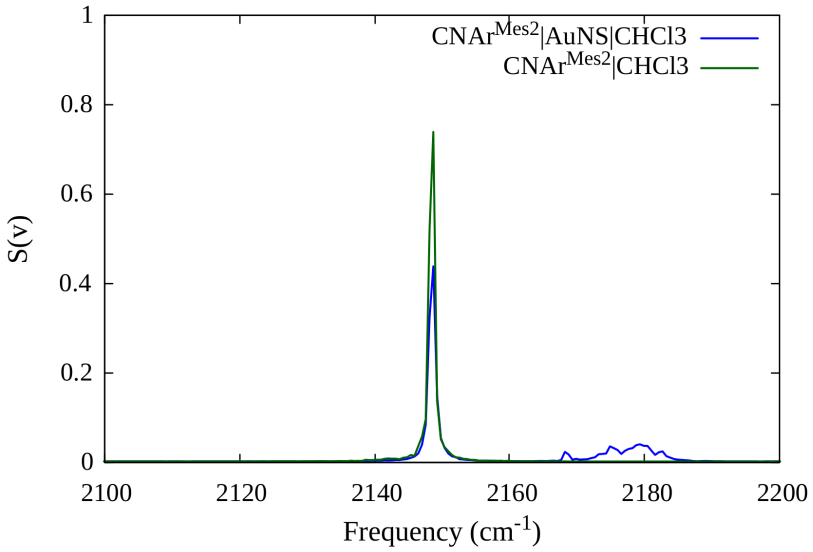

Fig. S13. Simulated C≡N vibrational spectrum of $CNAr^{Mes2}$ as a free molecule in $CHCl_3$ (green) and as a bound-molecule to the AuNSs surface (blue). A blueshift of ~ 30 cm^{-1} is observed upon binding, in good agreement with both experimental FTIR and surface-enhanced Raman spectroscopic (SERS) data.

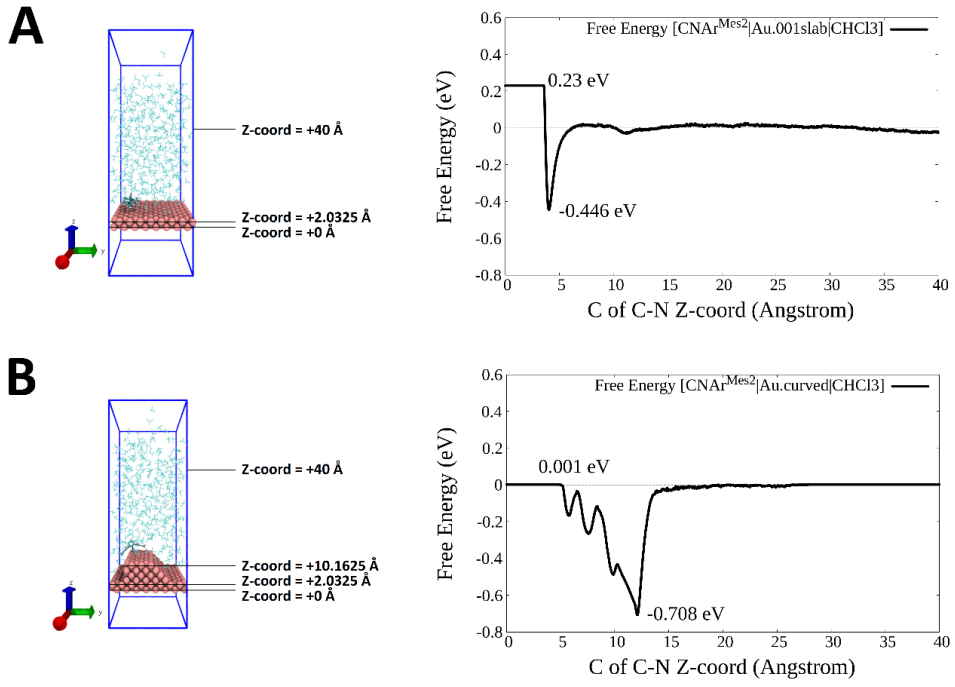

Fig. S14. Free energy of binding of $CNAr^{Mes2}$ to (A) Au(001) slab and (B) Au(curved) slab. All calculations employed Metadynamics accelerated sampling in $CHCl_3$ at 298K. The distance, Z, was computed between the carbon of $CNAr^{Mes2}$ C≡N group and the bottom of the Au-slab (Z coordinate = 0 Å).

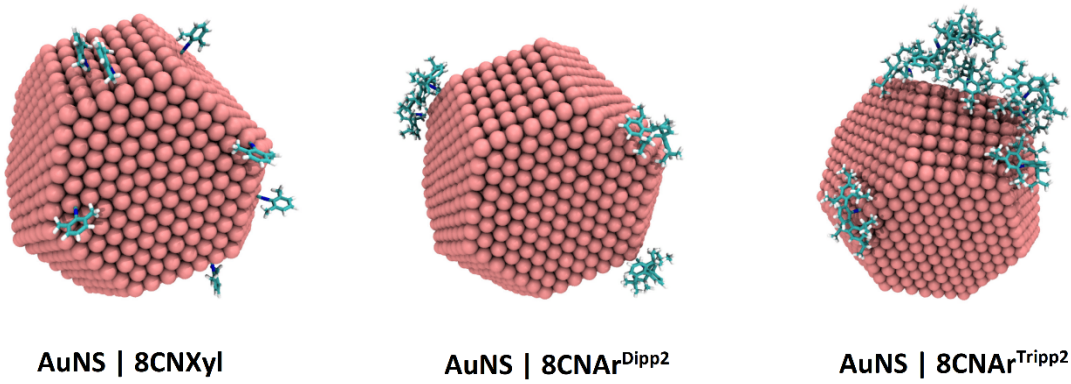

Fig. S15. Final snapshot from equilibrium MD simulations in vacuum at 298K of (left to right) CNXyl, $CNAr^{Dipp2}$, $CNAr^{Tripp2}$ on a 5nm AuNS.

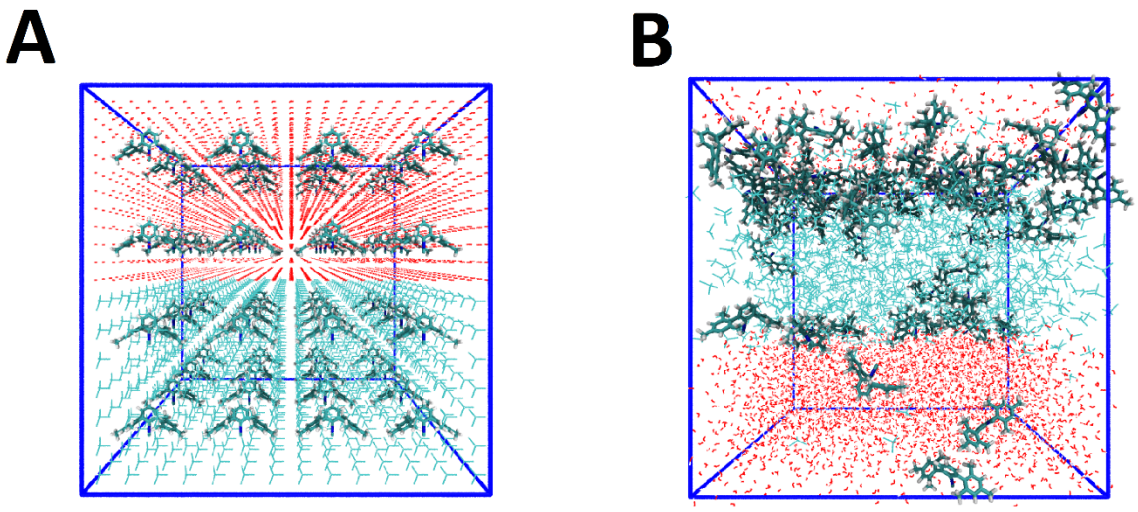

Fig. S16. (**A**) Initial snapshot of 64 $CNAr^{Mes2}$ molecules randomly distributed in a box containing 4484 water molecules (red) and 1096 $CHCl_3$ molecules (blue). (**B**) Final snapshot after equilibrium MD simulation at 298K and 1atm, showing $CNAr^{Mes2}$ ligands transferring to the organic $CHCl_3$ phase.

S4. Supplementary Tables.

Table S1. Simulated and experimental isocyanide stretching frequencies, ν(CN), of Au-bound and free $CNAr^{Mes2}$.

Simulated ν(CN) in $CHCl_3$		**Experimental ν(CN)**	
Free $CNAr^{Mes2}$	Adsorbed $CNAr^{Mes2}$	Free $CNAr^{Mes2}$	Adsorbed $CNAr^{Mes2}$
2149 cm^{-1}	2170-2185 cm^{-1}	2119 cm^{-1} (FTIR)	2166.5 cm^{-1} (SERS)

Table S2. Solvation free energies difference of various Isocyanide ligands in $CHCl_3$ and water, and cohesive free energy (self-solvation energy) from Free Energy Perturbation calculations.

Ligand	$\mathbf{A_{ligand\|CHCl3}}$ **(eV)**	$\mathbf{A_{ligand\|water}}$ **(eV)**	$\mathbf{A_{cohesive}}$ **(eV)**
CNXyl	-0.24	-0.01	0.06
$CNAr^{Dipp2}$	-0.83	0.04	-0.44
$CNAr^{Mes2}$	-1.01	-0.37	-0.62
$CNAr^{Tripp2}$	-0.90	0.09	-0.52

Table S3. Values of computational descriptors for various isocyanide ligands.

Ligand	**SBR**	**EBF**	**SF**	**SPF**
CNXyl	0.22	0.43	-0.02	0.23
$CNAr^{Dipp2}$	0.60	-0.14	0.40	0.87
$CNAr^{Mes2}$	1.00	0.12	0.28	0.52
$CNAr^{Tripp2}$	0.46	-0.52	0.38	1.00

Table S4. Composition of simulation cells used in various MD simulations. The associated figures are indicated.

System	Ligand(s)	# of Ligands	# of AuNSs	# $CHCl_3$
$CNAr^{Mes2}$ on AuNS (**Fig.1B**)	$CNAr^{Mes2}$	8	1	0 (Vacuum)
$CNAr^{Mes2}$-AuNS in $CHCl_3$ (**Fig. 2**)	$CNAr^{Mes2}$	106	1	7337
Isocyanides on AuNS (**Fig. S15**)	CNXyl, $CNAr^{Dipp2}$, $CNAr^{Tripp2}$	8	1	0 (Vacuum)

S5. References.

1. Fox, B. J.; Sun, Q. Y.; Dipasquale, A. G.; Fox, A. R.; Rheingold, A. L.; Figueroa, J. S., Solution behavior and structural properties of Cu(I) complexes featuring m-terphenyl isocyanides. *Inorganic Chemistry* **2008,** *47* (19), 9010-9020.
2. Ditri, T.; Fox, B.; Moore, C.; Rheingold, A.; Figueroa, J., Effective Control of Ligation and Geometric Isomerism: Direct Comparison of Steric Properties Associated with Bis-mesityl and Bis-diisopropylphenyl m-Terphenyl Isocyanides. *Inorganic Chemistry* **2009,** *48* (17), 8362-8375.
3. Carpenter, A. E.; Mokhtarzadeh, C. C.; Ripatti, D. S.; Havrylyuk, I.; Kamezawa, R.; Moore, C. E.; Rheingold, A. L.; Figueroa, J. S., Comparative Measure of the Electronic Influence of Highly Substituted Aryl Isocyanides. *Inorganic Chemistry* **2015,** *54* (6), 2936-2944.
4. Bastús, N. G.; Comenge, J.; Puntes, V., Kinetically controlled seeded growth synthesis of citrate-stabilized gold nanoparticles of up to 200 nm: size focusing versus Ostwald ripening. *Langmuir* **2011,** *27* (17), 11098-11105.
5. Kimling, J.; Maier, M.; Okenve, B.; Kotaidis, V.; Ballot, H.; Plech, A., Turkevich method for gold nanoparticle synthesis revisited. *The Journal of Physical Chemistry B* **2006,** *110* (32), 15700-15707.
6. Liu, X.; Atwater, M.; Wang, J.; Huo, Q., Extinction coefficient of gold nanoparticles with different sizes and different capping ligands. *Colloids and Surfaces B: Biointerfaces* **2007,** *58* (1), 3-7.
7. Shao, Y.; Gan, Z.; Epifanovsky, E.; Gilbert, A. T.; Wormit, M.; Kussmann, J.; Lange, A. W.; Behn, A.; Deng, J.; Feng, X., Advances in molecular quantum chemistry contained in the Q-Chem 4 program package. *Mol. Phys.* **2015,** *113*, 184-215.
8. Giannozzi, P.; Baroni, S.; Bonini, N.; Calandra, M.; Car, R.; Cavazzoni, C.; Ceresoli, D.; Chiarotti, G. L.; Cococcioni, M.; Dabo, I.; Corso, A. D.; Gironcoli, S. d.; Fabris, S.; Fratesi, G.; Gebauer, R.; Gerstmann, U.; Gougoussis, C.; Kokalj, A.; Lazzeri, M.; Martin-Samos, L.; Marzari, N.; Mauri, F.; Mazzarello, R.; Paolini, S.; Pasquarello, A.; Paulatto, L.; Sbraccia, C.; Scandolo, S.; Sclauzero, G.; Seitsonen, A. P.; Smogunov, A.; Umari, P.; Wentzcovitch, R. M., QUANTUM ESPRESSO: a modular and open-source software project for quantum simulations of materials. *J. Phys.: Condens. Matter* **2009,** *21*, 395502.
9. Giannozzi, P.; Andreussi, O.; Brumme, T.; Bunau, O.; Nardelli, M. B.; Calandra, M.; Car, R.; Cavazzoni, C.; Ceresoli, D.; Cococcioni, M.; Colonna, N.; Carnimeo, I.; Corso, A. D.; Gironcoli, S. d.; Delugas, P.; Jr, R. A. D.; Ferretti, A.; Floris, A.; Fratesi, G.; Fugallo, G.; Gebauer, R.; Gerstmann, U.; Giustino, F.; Gorni, T.; Jia, J.; Kawamura, M.; Ko, H.-Y.; Kokalj, A.; Küçükbenli, E.; Lazzeri, M.; Marsili, M.; Marzari, N.; Mauri, F.; Nguyen, N. L.; Nguyen, H.-V.; Otero-de-la-Roza, A.; Paulatto, L.; Poncé, S.; Rocca, D.; Sabatini, R.; Santra, B.; Schlipf, M.; Seitsonen, A. P.; Smogunov, A.; Timrov, I.;

Thonhauser, T.; Umari, P.; Vast, N.; Wu, X.; Baroni, S., Advanced capabilities for materials modelling with Quantum ESPRESSO. *J. Phys.: Condens. Matter* **2017,** *29*, 465901.

10. Plimpton, S., Fast Parallel Algorithms for Short-Range Molecular Dynamics. *J. Comp. Phys.* **1995,** *117*, 1-19.
11. Ackland, G. J.; Tichy, G.; Vitek, V.; Finnis, M. W., Simple N-body potentials for the noble metals and nickel. *Philosophical Magazine A* **1987,** *56* (6), 735-756.
12. Wang, J.; Wolf, R. M.; Caldwell, J. W.; Kollman, P. A.; Case, D. A., Development and testing of a general amber force field. *J Comput Chem* **2004,** *25* (9), 1157-74.
13. Kaminski, G. A.; Friesner, R. A.; Tirado-Rives, J.; Jorgensen, W. L., Evaluation and reparametrization of the OPLS-AA force field for proteins via comparison with accurate quantum chemical calculations on peptides. *The Journal of Physical Chemistry B* **2001,** *105* (28), 6474-6487.
14. Kamath, G.; Georgiev, G.; Potoff, J. J., Molecular Modeling of Phase Behavior and Microstructure of Acetone-Chloroform-Methanol Binary Mixtures. *J. Phys. Chem. B* **2005,** *109,* 19463-19473.
15. Mark, P.; Nilsson, L., Structure and Dynamics of the TIP3P, SPC, and SPC/E Water Models at 298 K. *J. Phys. Chem. A* **2001,** *105*, 9954-9960.
16. Karg, M.; Schelero, N.; Oppel, C.; Gradzielski, M.; Hellweg, T.; von Klitzing, R., Versatile phase transfer of gold nanoparticles from aqueous media to different organic media. *Chemistry* **2011,** *17* (16), 4648-54.
17. Hockney; Eastwood, Computer Simulation Using Particles. *Adam Hilger, NY* **1989**.
18. Shinoda, W.; Shiga, M.; Mikami, M., Rapid estimation of elastic constants by molecular dynamics simulation under constant stress. *Physical Review B* **2004,** *69* (13), 134103.
19. Martyna, G. J.; Tobias, D. J.; Klein, M. L., Constant pressure molecular dynamics algorithms. *The Journal of Chemical Physics* **1994,** *101* (5), 4177-4189.
20. Parrinello, M.; Rahman, A., Polymorphic transitions in single crystals: A new molecular dynamics method. *J. Appl. Phys.* **1981,** *52* (12), 7182-7190.
21. Tuckerman, M. E.; Alejandre, J.; López-Rendón, R.; Jochim, A. L.; Martyna, G. J., A Liouville-operator derived measure-preserving integrator for molecular dynamics simulations in the isothermal–isobaric ensemble. *J. Phys. A: Math. Gen.* **2006,** *39* (19), 5629.
22. Pascal, T. A.; Schärf, D.; Jung, Y.; Kühne, T. D., On the absolute thermodynamics of water from computer simulations: A comparison of first-principles molecular dynamics, reactive and empirical force fields. *J. Chem. Phys.* **2012,** *137*, 244507.
23. Chen, A. A.; Do, A.; Pascal, T. A., The Phase Diagram of Carbon Dioxide from Correlation Functions and a Many-body Potential. *J. Chem. Phys.* **2021,** *155*, 024503.
24. Zwanzig, R. W., High-Temperature Equation of State by a Perturbation Method. I. Nonpolar Gases. *The Journal of Chemical Physics* **1954,** *22*, 1420.
25. Liu, H.; Holoubek, J.; Zhou, H.; Chen, A.; Chang, N.; Wu, Z.; Yu, S.; Yan, Q.; Xing, X.; Li, Y.; Pascal, T. A.; Liu, P., Ultrahigh coulombic efficiency electrolyte enables Li||SPAN batteries with superior cycling performance. *Materials Today* **2021,** *42*, 17-28.
26. Mahinthichaichan, P.; Vo, Q. N.; Ellis, C. R.; Shen, J., Kinetics and Mechanism of Fentanyl Dissociation from the μ-Opioid Receptor. *American Chemical Society* **2021,** *1*, 2208-2215.